JACS
JOURNAL OF THE AMERICAN CHEMICAL SOCIETY
Article
pubs.acs.org/JACS

Importance of Reducing Vapor Atmosphere in the Fabrication of Tin-Based Perovskite Solar Cells

Tze-Bin Song,[†] Takamichi Yokoyama,[†,‡] Constantinos C. Stoumpos,[†] Jenna Logsdon,[†] Duyen H. Cao,[†] Michael R. Wasielewski,[†] Shinji Aramaki,[‡] and Mercouri G. Kanatzidis*[,†]

[†]Department of Chemistry, Northwestern University, 2145 Sheridan Road, Evanston, Illinois 60208, United States
[‡]Mitsubishi Chemical Group Science & Technology Research Center, Inc., 1000 Kamoshida-cho, Aoba-ku, Yokohama 227-8502, Japan

Supporting Information

ABSTRACT: Tin-based halide perovskite materials have been successfully employed in lead-free perovskite solar cells, but the tendency of these materials to form leakage pathways from p-type defect states, mainly Sn^{4+} and Sn vacancies, causes poor device reproducibility and limits the overall power conversion efficiencies (PCEs). Here, we present an effective process that involves a reducing vapor atmosphere during the preparation of Sn-based halide perovskite solar cells to solve this problem, using $MASnI_3$, $CsSnI_3$, and $CsSnBr_3$ as the representative absorbers. This process enables the fabrication of remarkably improved solar cells with PCEs of 3.89%, 1.83%, and 3.04% for $MASnI_3$, $CsSnI_3$, and $CsSnBr_3$, respectively. The reducing vapor atmosphere process results in more than 20% reduction of Sn^{4+}/Sn^{2+} ratios, which leads to greatly suppressed carrier recombination, to a level comparable to their lead-based counterparts. These results mark an important step toward a deeper understanding of the intrinsic Sn-based halide perovskite materials, paving the way to the realization of low-cost and lead-free Sn-based halide perovskite solar cells.

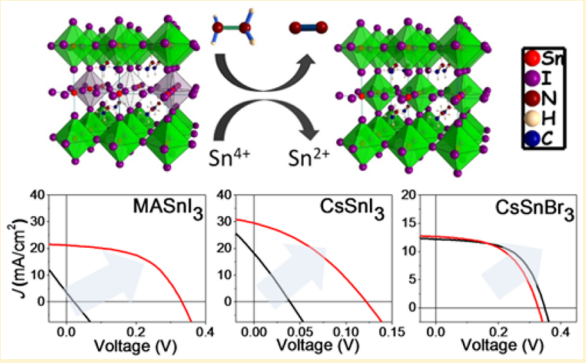

INTRODUCTION

In the past few years, organic−inorganic lead halide perovskites in the form of $APbX_3$ (A = cesium (Cs), methylammonium (MA), and formamidinium (FA); X = I, Br, and Cl) have attracted significant attention as promising materials for highly efficient and low-cost optoelectronic devices, such as lasers, light emitting diodes, and photodetectors.[1−3] These materials exhibit a number of remarkable properties, including long carrier diffusion lengths (>100 μm),[4] tunable bandgaps (E_g = 1.45−2.4 eV), and high absorption coefficients (>10^5 cm^{-1}).[5−7] Solar cells based on these materials have seen a sharp increase in efficiency, with certified power conversion efficiency (PCE) over 20% achieved in less than a decade of development.[8−11] The use of the toxic element lead, however, could be a major concern for large-scale deployment. Therefore, substituting Pb with environmentally benign elements could greatly increase its potential for practical application and production.

An obvious step in this direction is the substitution of Pb with its group 14 congeners, tin or germanium, that can retain the three-dimensional (3D) perovskite framework.[12−15] Other perovskite derivatives, such as 2D perovskite $Cs_3Sb_2I_9$ and the molecular $Cs_3Bi_2I_9$ iodobismuthate analogue, as well as the ordered double perovskites Cs_2AgBiX_6 and $Cs_2Sn_{1-x}I_6$, have been recently explored.[16−20] Among them, the Sn-based halide perovskites hold particular promise with respect to their device performance. In general, the Sn-based halide perovskites exhibit smaller E_g (~1.2 eV) than their Pb counterparts, with an absorption edge lying in the near-infrared region (900−1000 nm), thus having a great potential as superior light-absorbing materials for high-performance solar cells, tandem cells, and photodetector devices.[21−23] Until now, however, the Sn-based halide perovskite devices have suffered from a few fundamental limitations, with the most important one being the facile oxidation of Sn^{2+} to Sn^{4+} when exposed in air or even in a glovebox with trace amounts of water and oxygen (<10 ppm). This "self-doping" effect enabled the first use of perovskite, $CsSnI_3$, as a hole transport material in a solid-state dye-sensitized solar cell.[24] Due to the self-doping effect, however, rapid degradation and poor reproducibility are observed in fabricated devices using tin-based perovskites as absorbers.[25−29] In order to suppress the instability of Sn^{2+}, recent studies have focused on the artificial stabilization of the favorable divalent state, such as by adding 20 mol% of SnF_2 in the precursor solution or forming an intermediate SnF_2−pyrazine complex, where in both cases the fluoride ions act as a stabilizer against oxidation (SnF_2 is air- and moisture-stable).[30−33] The disadvantage of these approaches is that excess SnF_2 could potentially result in poor film morphologies and device performances.[26,27,29]

Received: October 17, 2016
Published: December 15, 2016

DOI: 10.1021/jacs.6b10734
J. Am. Chem. Soc. 2017, 139, 836−842

Here, we introduce a novel and effective reducing vapor atmosphere method using hydrazine as the vapor to improve the quality of the Sn-based halide perovskite films/materials. Hydrazine is widely known as a strong reducing agent and also a strong base which could potentially prevent or suppress the high-oxidation Sn^{4+} formation. Moreover, hydrazine has high volatility, which makes it easy to introduce and remove without the need for high annealing temperatures. To examine the effectiveness and the universality of our approach, three different materials, $MASnI_3$, $CsSnI_3$, and $CsSnBr_3$, were studied. Instead of incorporating hydrazine directly into the perovskite solution, which often results in unfavorable over-reduction of the Sn^{4+}, a vapor reaction affords a finer control over the reaction process. We observe significant improvement in device performance with all three materials, and a possible mechanism highlighting the chemical interactions between the hydrazine vapor and Sn-based perovskites is proposed. Further characterizations on the perovskite films support the suppression of the Sn^{4+} species, such as the observations of enhanced carrier lifetimes and lowered recombination rate constants when hydrazine vapor is used. Significantly improved PCEs are achieved for the respective materials, with 3.89% for $MASnI_3$, 1.83% for $CsSnI_3$, and record-high 3.04% for $CsSnBr_3$.

EXPERIMENTAL SECTION

Materials. Cesium iodide (CsI), cesium bromide (CsBr), tin fluoride (SnF_2), poly[bis(4-phenyl)(2,4,6-trimethylphenyl)amine] (PTAA), mesoporous TiO_2 (mp-TiO_2) paste (Dyesol DSL 18NR-T), hydrazine, titanium isopropylate (TTIP), chlorobenzene (CB), and dimethyl sulfoxide (DMSO) were obtained from Sigma-Aldrich. Methylammonium iodide (CH_3NH_3I, MAI) was purchased from 1-Materials Inc. Tin bromide ($SnBr_2$) and tetrakis(pentafluorophenyl)-borate (TPFB) were purchased from Alfa Aesar and Tokyo Chemical Industry Co, Ltd., respectively. Fluorine-doped tin oxide (FTO)-coated glass (TEC7, 2.2 mm) was purchased from Hartford Glass Co. Inc. Tin iodide (SnI_2) was prepared according to a previous report.[35] Low-temperature thermoplastic sealant (Dyesol Ltd.) was purchased for the encapsulation process.

Device Fabrication. Solutions of 0.8 M concentration of $MASnI_3$, $CsSnI_3$, and $CsSnBr_3$ were prepared by dissolving SnI_2 or $SnBr_2$ with MAI or CsI/CsBr in DMSO solution, and 20 mol% SnF_2 was added to the solution. The mixture solutions were heated at 150 °C to get all compounds fully dissolved. A compact TiO_2 layer (c-TiO_2) was prepared by the sol–gel method as previously reported on pre-patterned FTO-coated glass, followed by 500 °C annealing for 20 min. Mp-TiO_2 paste was diluted with anhydrous ethanol (1:3.5 weight ratio) and spin-coated onto c-TiO_2/FTO substrates, followed by 500 °C annealing for 15 min. The thickness of the mp-TiO_2 layer can be adjusted by varying the spin speed or increasing the coating cycles. The substrates were treated with 0.02 M aqueous $TiCl_4$ solution at 70 °C for 1 h, washed with ethanol and DI water, and then annealed at 500 °C for 15 min. The hot $MASnI_3$/$CsSnI_3$/$CsSnBr_3$ solution was dropped onto glass/FTO/c-TiO_2/mp-TiO_2 substrates at 150 °C, immediately followed by 1500 rpm spinning for 30 s. Various amounts of hydrazine solution were dropped onto a blank glass substrate spinning at 1500 rpm. The blank glass substrate was spinned for at least another 5 min to promote the vaporization of the hydrazine. Next, deposition of the perovskite layer was performed. ***Caution!*** *Hydrazine must be handled using appropriate protective equipment to prevent physical contact with either vapor or liquid.* The $MASnI_3$/$CsSnI_3$/$CsSnBr_3$ films were post-annealed at 100 °C for 20 min. PTAA with TPFB organic dopant (9:1 weight ratio) dissolved in CB was deposited on the perovskite film by spin-coating at 1500 rpm for 30 s, followed by annealing at 70 °C for 5 min, as hole transport layer (HTL). Finally, 100-nm-thick gold top electrodes were thermally evaporated on top of the film through metal mask. Thermoplastic sealants with glass slides were applied to encapsulate the active area of the devices, as shown in the insets of Figure 5, before characterization.

Characterization. Current density–voltage (J–V) characteristics were measured under AM1.5G light (100 mW/cm^2) using the xenon arc lamp of a Spectra-Nova Class A solar simulator. Light intensity was calibrated using an NREL-certified monocrystalline Si diode coupled to a KG3 filter to bring spectral mismatch to unity. A Keithley 2400 source meter was used for electrical characterization. The device area was between 0.12 and 0.15 cm^2, defined by the overlapping area between the un-etched FTO glass and Au electrode. Photocurrent density was confirmed with the black shadow mask. Incident photon conversion efficiencies (IPCEs) were characterized using an Oriel model QE-PV-SI instrument equipped with a NIST-certified Si diode. Monochromatic light was generated from an Oriel 300-W lamp. The transmittance spectra were taken using a Shimadzu ultraviolet–visible spectrophotometer (UV-3600). X-ray photoelectron spectroscopy (XPS) measurements were carried out on an Omicron ESCA Probe XPS spectrometer (Thermo Scientific ESCALAB 250Xi) using 150 eV pass energy and 1 eV step size for survey scan and 20 eV pass energy and 0.01 eV step size for fine scan. Surface etching was performed by Ar-ion sputtering with 1 keV accelerating for 15 s. Scanning electron microscopy (SEM) images were taken on a Hitachi SU8030 electron microscope, and X-ray diffraction (XRD) spectra were collected using Rigaku MiniFlex600 X-ray diffractometer (Cu Kα, 1.5406 Å). Time-resolved fluorescence data were collected at room temperature using a streak camera system (Hamamatsu C4334 Streakscope). Laser pulses of 515 nm were utilized as the excitation source, which were generated by the same high repetition rate (100 kHz) ultrafast laser system. The absorption coefficient (α) is estimated according to the following equation:

$$\alpha = -\frac{\ln(1 - T - R)}{L} \tag{1}$$

where T is the transmission, R is the reflection of the film, and L is the average film thickness obtained from the high-resolution stylus profilometer (Veeco Dektak 150 surface profiler).

The initial photogenerated carrier density (N_0) used in the transient absorption and time-resolved fluorescence measurements is obtained according to the following equation:

$$N_0 = \varphi \frac{E\lambda}{hc} \frac{e^{-\alpha L}}{L} \tag{2}$$

where E is the energy in a single excitation pulse of wavelength λ, α is the absorption coefficient obtained from eq 1, L is the average film thickness, and φ is the ratio of free charge carriers created per photon absorbed (assumed to be unity).

RESULTS AND DISCUSSION

Three Sn-based halide perovskite solutions, i.e., $MASnI_3$, $CsSnI_3$, and $CsSnBr_3$ (from top to bottom shown in Figure 1a), were prepared by mixing AX (A = MA or Cs; X = I or Br) and SnX_2 (X = I or Br) with 20 mol% of SnF_2 in DMSO and heating at 150 °C to obtain clear solutions (Figure S1). Mesoporous TiO_2 (mp-TiO_2) substrates were preheated at 150 °C before film deposition. Hydrazine vapor was generated before the spin-coating process by dropping hydrazine solution into the spin-coater chamber. (Details are described in the Experimental Section.) Due to the high volatility of hydrazine (1 kP at room temperature), the vapor concentration can be reproducibly adjusted by changing the amount of hydrazine present in the spin-coater chamber. A schematic diagram of the deposition process is shown in Figure 1a, where hot solutions were cast onto hot substrates, followed immediately by the spinning process. The films turned to their corresponding colors right after spinning and were post-annealed at 100 °C for 10 min to achieve better crystallinity and remove residual solvents. All films presented here, irrespective of the presence

DOI: 10.1021/jacs.6b10734
J. Am. Chem. Soc. 2017, 139, 836–842

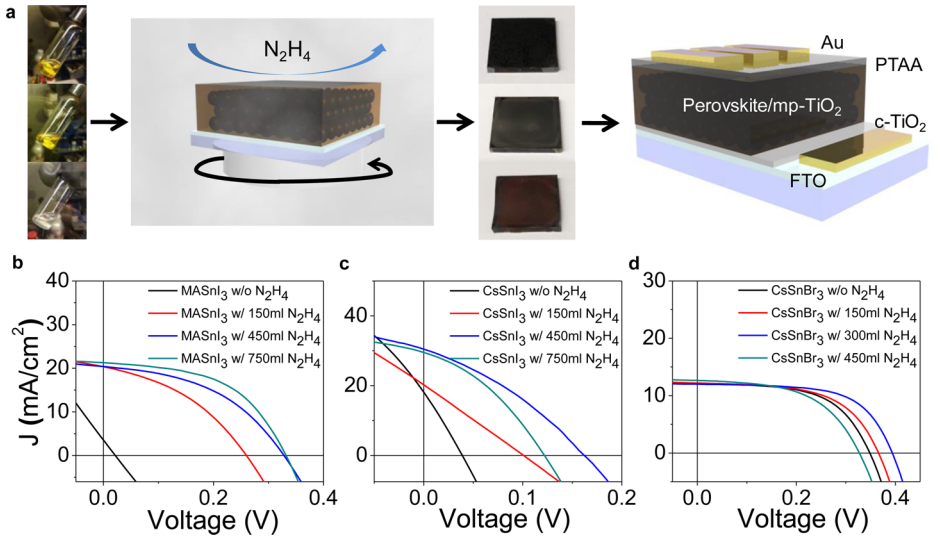

Figure 1. Top: Scheme of reducing vapor atmosphere process of device fabrication and photovoltaic performances. (a) Reducing vapor atmosphere procedure for preparing $MASnI_3$ (top), $CsSnI_3$ (middle), and $CsSnBr_3$ (bottom) perovskite solar cell devices and device structure (glass/FTO/c-TiO_2/mp-TiO_2-perovskite/perovskite capping layer/PTAA/Au). Bottom: Representative J–V curves for (b) $MASnI_3$ solar cells, (c) $CsSnI_3$ solar cells, and (d) $CsSnBr_3$ solar cells without and with various hydrazine vapor concentrations.

or absence of hydrazine vapor, show good coverage on top of the mp-TiO_2 layer, as shown in the top-view SEM images (Figure S2). XRD patterns also show no significant change in the film growth direction, with the perovskite orienting along the (001) direction in all cases (Figure S3). Moreover, from the absorption spectra, there are no observable changes in the E_g ($MASnI_3$ ~1.30 eV, $CsSnI_3$ ~1.25 eV, and $CsSnBr_3$ ~1.79 eV) when hydrazine vapor is used, but the absorption edge becomes sharper in all three cases (Figure S4). The sharper optical absorption edge indicates less disorder and defects; hence, better optical response could be expected.[34] After post-annealing, PTAA doped with TPFB and Au metal were deposited on the active layer as HTL material and photocathode, respectively, to complete the device fabrication.

Representative current density–voltage (J–V) curves with various amount of hydrazine solution in the spin coater are shown in Figure 1b, and the corresponding PCEs are shown in Figure S5. All devices show significant PCE improvement when hydrazine vapor is employed. In previous reports for $MASnI_3$ and $CsSnI_3$, several factors have been suggested to account for the excess p-doping, even shorting behavior in devices, including the impurity of the SnI_2 starting material and unexpected defect formation as well as oxidized Sn (Sn^{4+}) impurity.[25,26,29,37] Without the hydrazine vapor reaction, we obtain similar results, with $MASnI_3$ and $CsSnI_3$ devices showing near shorting behavior, even with the SnF_2 additive. However, with proper amounts of hydrazine vapor, the PCEs of $MASnI_3$ and $CsSnI_3$ devices were improved dramatically, from an average of ~0.02% to 3.40% and ~0.16% to 1.50%, respectively. This trend is also observed in $CsSnBr_3$ devices, increasing from ~2.36% to 2.82%, mainly due to the improved open-circuit voltage (V_{OC}). To demonstrate the reproducibility of the presented method, the device statistics of $CsSnBr_3$ devices are shown in Figure S6. One thing to note is that $CsSnBr_3$ is more stable than the other two perovskites, and it is not required to encapsulate the $CsSnBr_3$ devices for measurements in air for a short time; the device air-stability is shown in Figure S7. It has been reported that $MASnI_3$ and $CsSnI_3$ are very unstable in air, and even $MASnBr_3$ degrades significantly after 30 min of air exposure.[29,32,36] Remarkably, $CsSnBr_3$ devices can last for hours without losing the diode characteristics, as shown in Figure S7c, making it an attractive material for further investigations.

On the basis of chemical interactions between hydrazine and Sn-based halide perovskites, we propose a possible reaction mechanism responsible for the observed performance change with schematic diagrams shown in Figure 2. As mentioned

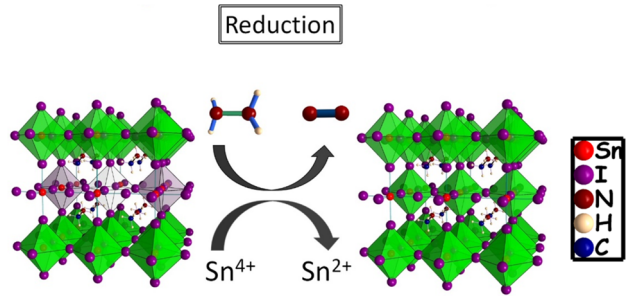

Figure 2. Proposed possible mechanism of hydrazine vapor reaction with Sn-based perovskite materials. Reduction process: $2SnI_6^{2-} + N_2H_4 \rightarrow 2SnI_4^{2-} + N_2 + 4HI$.

previously, hydrazine is well recognized as a strong reagent to reduce metal salts and metal oxides to pure metals, as well as an oxygen scavenger ($N_2H_4 + O_2 \rightarrow N_2 + 2H_2O$) to decrease surrounding oxygen levels. With these points in mind, we chose to use hydrazine in its vapor form, instead of directly adding it into the perovskite precursor solutions, to prevent the full reduction of Sn halide salts to Sn metal. Therefore, by generating the more diluted (relative to the form in solution) hydrazine atmosphere during the device fabrication process, not only the Sn^{4+} impurities could be reduced but also the unfavorable reduction of Sn^{2+} could be suppressed.

The possible reaction path during the thin-film formation is given as $2SnI_6^{2-} + N_2H_4 \rightarrow 2SnI_4^{2-} + N_2 + 4HI$, shown in Figure 2. The reduction of Sn^{4+} to Sn^{2+} decreases the amount of Sn^{2+} vacancies (V_{Sn}), thus suppressing the undesirable p-type electrical conductivity and reverting the perovskites back to the desirable semiconducting behavior.[37] The smaller amount

DOI: 10.1021/jacs.6b10734
J. Am. Chem. Soc. 2017, 139, 836–842

of V_{Sn} would lead to decreased cation antisite (A_{Sn}) and anion antisite (X_{Sn}) formation, further contributing to a lower level of p-type doping.[38] This mechanism could account for the observed device performance improvements from shorting diodes to working diodes, especially in $MASnI_3$ and $CsSnI_3$, and better device performances in $CsSnBr_3$.

To further confirm the proposed mechanisms, we performed chemical state analysis and elemental analysis using XPS as shown in Figure 3 and Figure S8. As discussed above, Sn in the 4+ state is considered as the major source for impurity and defect formation in Sn-based halide perovskite materials. The Sn states from pristine $MASnI_3$, $CsSnI_3$, and $CsSnBr_3$ films are shown in Figure 3a. Sn3d peaks in $MASnI_3$, $CsSnI_3$, and $CsSnBr_3$ films are deconvoluted into Sn^{2+} and Sn^{4+} peaks, and the Sn^{4+}/Sn^{2+} ratios are calculated and shown in Figure 3b. The levels of Sn^{4+} are significantly smaller in all $MASnI_3$, $CsSnI_3$, and $CsSnBr_3$ films prepared under hydrazine vapor comparing to those without. The Sn^{4+}/Sn^{2+} ratios are reduced by 45.8%, 21.5%, and 20.8% in $MASnI_3$, $CsSnI_3$, and $CsSnBr_3$ films, respectively. To further confirm that the observed difference does not come from surface contamination, physically adsorbed species, or surface chemical reaction, argon ion etching of the surface was performed prior to characterizing the bulk properties. The Sn state spectra after etching are shown in Figure S8a, and the Sn^{4+}/Sn^{2+} ratios of all the films after etching are included in Figure 3b. Although the Sn^0 state was also observed after the etching process (which could be caused by a sputtering reduction and might affect the quantitative accuracy of the Sn^{4+}/Sn^{2+} ratio), a markedly smaller amount of the Sn^{4+} in the bulk of $MASnI_3$ and $CsSnI_3$ films are still observed. These results unambiguously verified that hydrazine vapor reaction can reduce or suppress the level of Sn^{4+}, which is crucial to achieving working devices as we demonstrated.

Time-resolved photoluminescence measurements of the $MASnI_3$, $CsSnI_3$, and $CsSnBr_3$ films prepared without and with hydrazine vapor reveal that those films with hydrazine vapor exhibit longer carrier lifetimes than without, as shown in Figure 4. To unravel the charge recombination rates associated with both first- and higher-order processes, we fit the decay curves with the following differential equation:

$$\frac{dN}{dt} = -k_1 N - k_2 N^2$$

where N is the photoinduced charge carrier density, and k_1 and k_2 are the first- and second-order recombination rate constants for monomolecular nonradiative (trap-assisted) and bimolecular charge-carrier radiative recombination, respectively. The monomolecular recombination lifetimes ($\tau_1 = k_1^{-1}$) of the three materials are enhanced significantly by 1.91 times (from 5.42 to 10.34 ns), 3.27 times (from 6.03 to 19.70 ns), and 2.95 times

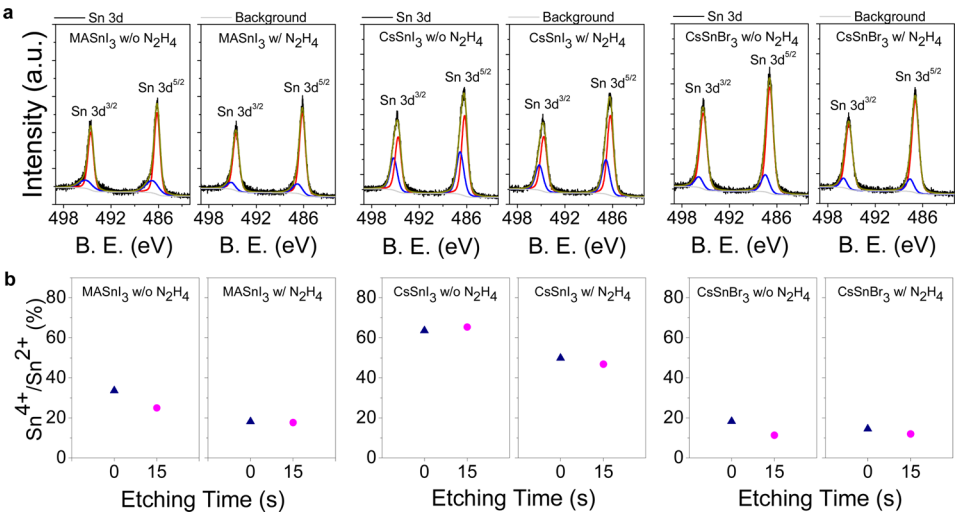

Figure 3. Chemical states of the Sn-based halide perovskite films. (a) XPS spectra of $MASnI_3$ (left), $CsSnI_3$ (middle), and $CsSnBr_3$ (right) perovskite films on mp-TiO_2 substrates prepared without and with hydrazine vapor and deconvolution curves. Measured results, black line; Sn^{2+} state, red line; Sn^{4+} state, blue line; background, gray line; sum of all deconvolution curves, gold line. (b) The obtained ratios of Sn^{4+}/Sn^{2+} of $MASnI_3$ (left), $CsSnI_3$ (middle), and $CsSnBr_3$ (right) films from the XPS spectra deconvolution in panel a and Figure S7, before and after Ar ion etching.

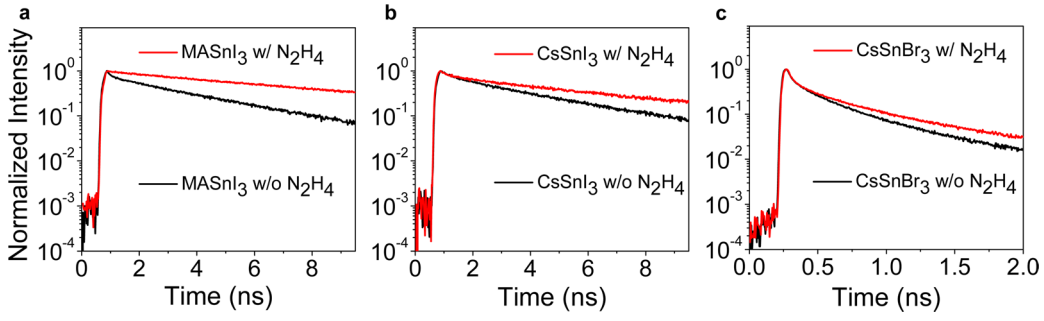

Figure 4. Charge recombination properties of Sn-based halide perovskite films. Time-resolved photoluminescence decay spectra of (a) $MASnI_3$, (b) $CsSnI_3$, and (c) $CsSnBr_3$ films prepared without and with hydrazine vapor on glass and measured with glass slide encapsulation.

DOI: 10.1021/jacs.6b10734
J. Am. Chem. Soc. 2017, 139, 836−842

(from 1.02 to 3.01 ns) in $MASnI_3$, $CsSnI_3$, and $CsSnBr_3$ films, respectively. The longer monomolecular charge-carrier lifetimes indicate smaller trap densities in the materials and smaller k_1 values, as shown in Table 1.[39] Moreover, these results also

Table 1. First- and Second-Order Charge Recombination Kinetics, with and without Hydrazine Vapor

	N_2H_4	τ_1 (ns)	k_1 (s^{-1})	k_2 ($cm^3\ s^{-1}$)
$MASnI_3$	w/o	5.42	1.84×10^8	9.57×10^{-9}
	w/	10.35	9.67×10^7	9.27×10^{-10}
$CsSnI_3$	w/o	6.03	1.66×10^8	8.74×10^{-9}
	w/	19.70	5.08×10^7	4.58×10^{-9}
$CsSnBr_3$	w/o	1.02	9.76×10^8	6.40×10^{-7}
	w/	3.01	3.32×10^8	3.94×10^{-7}

corroborate our XPS results showing a decreased level of Sn^{4+} impurities, and other defect states achieved through the hydrazine vapor reaction. The bimolecular recombination rate constants (k_2) of the three materials also decrease from 9.57×10^{-9} to 9.27×10^{-10} $cm^3\ s^{-1}$ in $MASnI_3$, 8.74×10^{-9} to 4.58×10^{-9} $cm^3\ s^{-1}$ in $CsSnI_3$, and 6.40×10^{-7} to 3.94×10^{-7} $cm^3\ s^{-1}$ in $CsSnBr_3$ films. In both $MASnI_3$ and $CsSnI_3$, the k_2 values are within the same order of magnitude as that of $MAPbI_3$ from previous reports.[40,41] Particularly, the $MASnI_3$ film prepared under hydrazine vapor shows similar k_1 and k_2 values to those of the $MAPbI_3$ films.[40] In $CsSnBr_3$, the longer carrier lifetime and fewer defect states support the V_{OC} improvement observed in the device results in Figure 1d. Based on these results, further improving the PCEs of these Sn-based halide perovskite solar cells up to a level similar to those of their Pb-based counterparts could be well within reach with further optimization of the device fabrication process.

The optimized device performances and IPCE spectra of $MASnI_3$, $CsSnI_3$, and $CsSnBr_3$ are shown in Figure 5, with corresponding device cross-sectional SEM images shown in Figure S9. For $MASnI_3$, devices with over 50% fill factor (FF) can be achieved consistently, and this FF value (Figure 5a) is the highest among all the current reports.[27−29,42,43,35] The higher FF value can be attributed to the suppressed p-type doping and leakage pathways, which in turn led to a higher shunt resistance. The four-point probe technique was employed to measure the resistance of the thin films prepared with and without reducing vapor atmosphere. It was clearly observed that the films prepared in the reducing vapor atmosphere have significantly higher resistance than the ones without as shown in Figure S10. This result supports the lower p-type doping level for the films prepared under reducing vapor atmosphere that results in FF improvement in device performance. From the IPCE spectrum of $MASnI_3$ shown in Figure 5d, poor photocurrent contributions near the band edge compared to those of $CsSnI_3$ and $CsSnBr_3$ devices are observed, indicating that the $MASnI_3$ has relatively low absorption near the band edge or limited carrier diffusion length. Therefore, although $MASnI_3$ has a smaller E_g than its analogous $MAPbI_3$ material, it is a challenge to achieve higher short-circuit current (J_{SC}) than that of $MAPbI_3$ devices.

The $CsSnI_3$ device shows the highest J_{SC} (over 30 mA/cm^2) among the three materials as shown in Figure 5b. A black shadow mask was used in all $J-V$ measurements to define the area of illumination and avoid overestimating the J_{SC}. However, the V_{OC} and FF values are still limited by the significant amount of Sn^{4+} in the films which could not be fully suppressed by the hydrazine vapor process as evident from XPS results. From the IPCE spectrum of $CsSnI_3$ device, it is surprising that the slope of the IPCE spectrum near band edge is ~7%/10 nm in Figure 5e, which is strikingly better than $MASnI_3$. However, the IPCE spectrum kept decreasing during measurement, due to reasons unclear at the moment, Figure S11. This causes the relatively large mismatch between the J_{SC} from $J-V$ measurement and the value from IPCE integration. The sharper slope of the IPCE spectrum near band edge suggests that $CsSnI_3$ has a better absorption coefficient near band edge or longer carrier diffusion length than $MASnI_3$ based on the ~1 μm thick mp-TiO_2 substrates as shown in Figure S9.

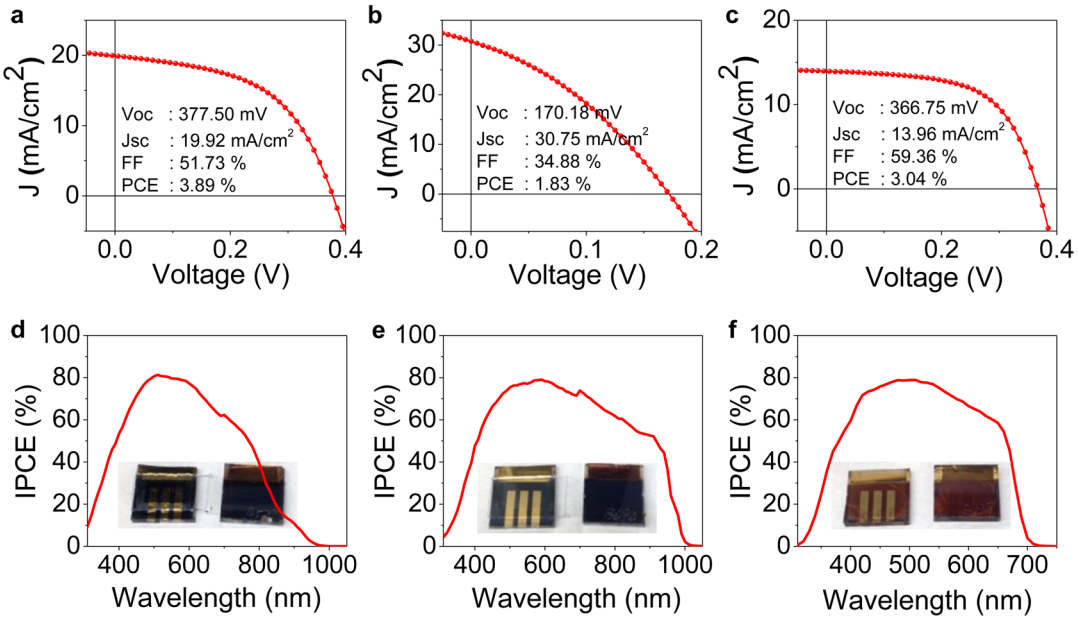

Figure 5. $J-V$ curves and IPCE of the best Sn-based halide perovskite cells. (a−c) The best $J-V$ curves of $MASnI_3$ (a), $CsSnI_3$ (b), and $CsSnBr_3$ (c). (d−f) The corresponding IPCE spectra of $MASnI_3$ (d), $CsSnI_3$ (e), and $CsSnBr_3$ (f) devices prepared with hydrazine vapor. The insets show the photos of corresponding Sn-based perovskite devices.

DOI: 10.1021/jacs.6b10734
J. Am. Chem. Soc. 2017, 139, 836−842

$CsSnBr_3$ devices exhibited a FF of near 60% and a highest PCE of over 3%, as shown in Figure 5c. $CsSnBr_3$ has an even sharper slope for the IPCE spectrum near band edge compared to $CsSnI_3$, with ~15%/10 nm (Figure 5f), approaching that of high performance Pb-based halide perovskite devices.[9] Comparing the properties of $CsSnI_3$ and $CsSnBr_3$ films, we expect that further reducing the level of Sn^{4+} and other defects in the $CsSnI_3$ films would improve not only the V_{OC} and FF values but also the IPCE response to give higher J_{SC} and higher performance Pb-free solar cells.

CONCLUSION AND PROSPECTS

We have demonstrated that incorporation of a hydrazine reducing vapor atmosphere process can lead to a universally dramatic increase in the power conversion efficiency of Sn-based perovskite solar cells for $MASnI_3$, $CsSnI_3$, and $CsSnBr_3$. The outstanding improvement is achieved by a combination of suppressed oxidized Sn^{4+} impurities and lowering levels of defect states by hydrazine vapor reactions. Eliminating the Sn^{4+} state is especially critical, as it is currently one of the main limiting factors for Sn-based perovskite systems, causing metallic-like highly doped p-type materials and shorting of devices. This work marks a milestone for lead-free perovskite solar cells, as it addresses the fundamental limitation of Sn-based perovskites and opens up new avenues of experimentation for achieving competitive and environmentally friendly alternatives to the prevalent Pb-based systems. Beyond improving the material quality, we believed that alternative device structures and electron transport layer (ETL) materials can be explored to achieve better band alignment between the ETL material and Sn-based perovskite materials. The present ETL/Sn-based perovskite interface is responsible for a major loss (>50%) of the device performance compared to Pb-based systems, which is suspected to be limited by the severe conduction band mismatch between the ETL TiO_2 and Sn-based perovskite material. Solving this problem would significantly improve the V_{oc} and FF values even further. Based on the approach presented here, further exploring the capacities of this emerging material system, as well as investigating the limitations on V_{OC} and stability of materials and devices, will bring us one step closer to achieving high-performance lead-free perovskite solar cells.

ASSOCIATED CONTENT

Supporting Information

The Supporting Information is available free of charge on the ACS Publications website at DOI: 10.1021/jacs.6b10734.

Experimental details; photographs of solutions; top-view SEM images of perovskite films; Tauc plots of perovskite films; XRD patterns of perovskite films with and without reducing atmosphere; device performances with various amounts of hydrazine vapor; device statistic results of $CsSnBr_3$ devices; $CsSnBr_3$ device stability; XPS spectra of perovskite films; cross-section SEM images of perovskite devices; resistance measurement of $MASnI_3$ films prepared with and without reducing atmosphere; and successive IPCE measurement of $CsSnI_3$ device (PDF)

AUTHOR INFORMATION

Corresponding Author

*m-kanatzidis@northwestern.edu

ORCID

Takamichi Yokoyama: 0000-0002-0766-4550

Constantinos C. Stoumpos: 0000-0001-8396-9578

Michael R. Wasielewski: 0000-0003-2920-5440

Notes

The authors declare no competing financial interest.

ACKNOWLEDGMENTS

T.-B.S. acknowledges financial support from Mitsubishi Chemical Group Science & Technology Research Center, Inc. D.H.C. acknowledges support from the Link Foundation through the Link Foundation Energy Fellowship Program. This work was supported in part by the ANSER Center, an Energy Frontier Research Center funded by the U.S. Department of Energy, Office of Science, Office of Basic Energy Sciences, under Award No. DE-SC0001059 (solar absorber material synthesis and solar cell characterization). This work made use of the EPIC facility (NUANCE Center-Northwestern University), which has received support from the MRSEC program (NSF DMR-1121262) at the Materials Research Center, and the Nanoscale Science and Engineering Center (EEC-0118025/003), both programs of the National Science Foundation; the State of Illinois; and Northwestern University.

REFERENCES

(1) Deschler, F.; Price, M.; Pathak, S.; Klintberg, L.; Jarausch, D. D.; Higler, R.; Huettner, S.; Leijtens, T.; Stranks, S. D.; Snaith, H. J.; Atature, M.; Phillips, R. T.; Friend, R. H. *J. Phys. Chem. Lett.* **2014**, *5*, 1421.

(2) Yuan, M.; Quan, L. N.; Comin, R.; Walters, G.; Sabatini, R.; Voznyy, O.; Hoogland, S.; Zhao, Y.; Beauregard, E. M.; Kanjanaboos, P.; Lu, Z.; Kim, D. H.; Sargent, E. H. *Nat. Nanotechnol.* **2016**, *11*, 872.

(3) Saidaminov, M. I.; Haque, M. A.; Savoie, M.; Abdelhady, A. L.; Cho, N.; Dursun, I.; Buttner, U.; Alarousu, E.; Wu, T.; Bakr, O. M. *Adv. Mater.* **2016**, *28*, 8144.

(4) Dong, Q.; Fang, Y.; Shao, Y.; Mulligan, P.; Qiu, J.; Cao, L.; Huang, J. *Science* **2015**, *347*, 967.

(5) Green, M. A.; Ho-Baillie, A.; Snaith, H. J. *Nat. Photonics* **2014**, *8*, 506.

(6) Yin, W.-J.; Shi, T.; Yan, Y. *Adv. Mater.* **2014**, *26*, 4653.

(7) Chen, Q.; De Marco, N.; Yang, Y.; Song, T.-B.; Chen, C.-C.; Zhao, H.; Hong, Z.; Zhou, H.; Yang, Y. *Nano Today* **2015**, *10*, 355.

(8) Kojima, A.; Teshima, K.; Shirai, Y.; Miyasaka, T. *J. Am. Chem. Soc.* **2009**, *131*, 6050.

(9) Jeon, N. J.; Noh, J. H.; Kim, Y. C.; Yang, W. S.; Ryu, S.; Seok, S. I. *Nat. Mater.* **2014**, *13*, 897.

(10) Zhou, H.; Chen, Q.; Li, G.; Luo, S.; Song, T.-B.; Duan, H.-S.; Hong, Z.; You, J.; Liu, Y.; Yang, Y. *Science* **2014**, *345*, 542.

(11) Jeon, N. J.; Noh, J. H.; Yang, W. S.; Kim, Y. C.; Ryu, S.; Seo, J.; Seok, S. I. *Nature* **2015**, *517*, 476.

(12) Stoumpos, C. C.; Kanatzidis, M. G. *Adv. Mater.* **2016**, *28*, 5778.

(13) Stoumpos, C. C.; Frazer, L.; Clark, D. J.; Kim, Y. S.; Rhim, S. H.; Freeman, A. J.; Ketterson, J. B.; Jang, J. I.; Kanatzidis, M. G. *J. Am. Chem. Soc.* **2015**, *137*, 6804.

(14) Saparov, B.; Mitzi, D. B. *Chem. Rev.* **2016**, *116*, 4558.

(15) Stoumpos, C. C.; Kanatzidis, M. G. *Acc. Chem. Res.* **2015**, *48*, 2791.

(16) Saparov, B.; Hong, F.; Sun, J.-P.; Duan, H.-S.; Meng, W.; Cameron, S.; Hill, I. G.; Yan, Y.; Mitzi, D. B. *Chem. Mater.* **2015**, *27*, 5622.

(17) Lehner, A. J.; Fabini, D. H.; Evans, H. A.; Hébert, C.-A.; Smock, S. R.; Hu, J.; Wang, H.; Zwanziger, J. W.; Chabinyc, M. L.; Seshadri, R. *Chem. Mater.* **2015**, *27*, 7137.

(18) McClure, E. T.; Ball, M. R.; Windl, W.; Woodward, P. M. *Chem. Mater.* **2016**, *28*, 1348.

(19) Lee, B.; Stoumpos, C. C.; Zhou, N.; Hao, F.; Malliakas, C.; Yeh, C.-Y.; Marks, T. J.; Kanatzidis, M. G.; Chang, R. P. H. *J. Am. Chem. Soc.* **2014**, *136*, 15379.

DOI: 10.1021/jacs.6b10734
J. Am. Chem. Soc. 2017, 139, 836−842

(20) Savory, C. N.; Walsh, A.; Scanlon, D. O. *ACS Energy Lett.* **2016**, *1*, 949.
(21) Stoumpos, C. C.; Malliakas, C. D.; Kanatzidis, M. G. *Inorg. Chem.* **2013**, *52*, 9019.
(22) Meillaud, F.; Shah, A.; Droz, C.; Vallat-Sauvain, E.; Miazza, C. *Sol. Energy Mater. Sol. Cells* **2006**, *90*, 2952.
(23) Donati, S. *Meas. Sci. Technol.* **2001**, *12*, 653.
(24) Chung, I.; Lee, B.; He, J. Q.; Chang, R. P. H.; Kanatzidis, M. G. *Nature* **2012**, *485*, 486.
(25) Takahashi, Y.; Obara, R.; Lin, Z.-Z.; Takahashi, Y.; Naito, T.; Inabe, T.; Ishibashi, S.; Terakura, K. *Dalton Trans.* **2011**, *40*, 5563.
(26) Takahashi, Y.; Hasegawa, H.; Takahashi, Y.; Inabe, T. *J. Solid State Chem.* **2013**, *205*, 39.
(27) Zuo, F.; Williams, S. T.; Liang, P.-W.; Chueh, C.-C.; Liao, C.-Y.; Jen, A. K. Y. *Adv. Mater.* **2014**, *26*, 6454.
(28) Wang, F.; Ma, J.; Xie, F.; Li, L.; Chen, J.; Fan, J.; Zhao, N. *Adv. Funct. Mater.* **2016**, *26*, 3417.
(29) Yokoyama, T.; Cao, D. H.; Stoumpos, C. C.; Song, T.-B.; Sato, Y.; Aramaki, S.; Kanatzidis, M. G. *J. Phys. Chem. Lett.* **2016**, *7*, 776.
(30) Kumar, M. H.; Dharani, S.; Leong, W. L.; Boix, P. P.; Prabhakar, R. R.; Baikie, T.; Shi, C.; Ding, H.; Ramesh, R.; Asta, M.; Graetzel, M.; Mhaisalkar, S. G.; Mathews, N. *Adv. Mater.* **2014**, *26*, 7122.
(31) Lee, S. J.; Shin, S. S.; Kim, Y. C.; Kim, D.; Ahn, T. K.; Noh, J. H.; Seo, J.; Seok, S. I. *J. Am. Chem. Soc.* **2016**, *138*, 3974.
(32) Sabba, D.; Mulmudi, H. K.; Prabhakar, R. R.; Krishnamoorthy, T.; Baikie, T.; Boix, P. P.; Mhaisalkar, S.; Mathews, N. *J. Phys. Chem. C* **2015**, *119*, 1763.
(33) Gupta, S.; Bendikov, T.; Hodes, G.; Cahen, D. *ACS Energy Lett.* **2016**, *1*, 1028.
(34) Donovan, T. M.; Spicer, W. E.; Bennett, J. M. *Phys. Rev. Lett.* **1969**, *22*, 1058.
(35) Hao, F.; Stoumpos, C. C.; Cao, D. H.; Chang, R. P. H.; Kanatzidis, M. G. *Nat. Photonics* **2014**, *8*, 489.
(36) Yokoyama, T.; Song, T.-B.; Cao, D. H.; Stoumpos, C. C.; Aramaki, S.; Kanatzidis, M. G. *ACS Energy Lett.* **2017**, *2*, 22.
(37) Chung, I.; Song, J.-H.; Im, J.; Androulakis, J.; Malliakas, C. D.; Li, H.; Freeman, A. J.; Kenney, J. T.; Kanatzidis, M. G. *J. Am. Chem. Soc.* **2012**, *134*, 8579.
(38) Xu, P.; Chen, S.; Xiang, H.-J.; Gong, X.-G.; Wei, S.-H. *Chem. Mater.* **2014**, *26*, 6068.
(39) Stranks, S. D.; Burlakov, V. M.; Leijtens, T.; Ball, J. M.; Goriely, A.; Snaith, H. J. *Phys. Rev. Appl.* **2014**, *2*, 034007.
(40) Wehrenfennig, C.; Eperon, G. E.; Johnston, M. B.; Snaith, H. J.; Herz, L. M. *Adv. Mater.* **2014**, *26*, 1584.
(41) Herz, L. M. *Annu. Rev. Phys. Chem.* **2016**, *67*, 65.
(42) Hao, F.; Stoumpos, C. C.; Guo, P.; Zhou, N.; Marks, T. J.; Chang, R. P. H.; Kanatzidis, M. G. *J. Am. Chem. Soc.* **2015**, *137*, 11445.
(43) Ogomi, Y.; Morita, A.; Tsukamoto, S.; Saitho, T.; Fujikawa, N.; Shen, Q.; Toyoda, T.; Yoshino, K.; Pandey, S. S.; Ma, T.; Hayase, S. *J. Phys. Chem. Lett.* **2014**, *5*, 1004.

DOI: 10.1021/jacs.6b10734
J. Am. Chem. Soc. 2017, 139, 836−842